Article

# Preparation of an $Fe_3O_4$ Nanoparticle/Carbonized Hemp Fiber Composite with Superior Microwave Absorption Performance

Wanxi Li,* Boqiong Li, Yali Zhao,* Yingfen Wang, Hengliang Liang, and Baoliang Lv

Cite This: *ACS Omega* 2024, 9, 48460−48470

Read Online

ACCESS | Metrics & More | Article Recommendations | Supporting Information

**ABSTRACT:** The increasing concern over the negative impact of electromagnetic radiation and interference on humans has led to a growing interest in microwave-absorbing materials that are cost-effective, have a wide frequency range, and have high efficiency. In this paper, an $Fe_3O_4$ nanoparticle/carbonized hemp fiber composite was successfully prepared using hemp fibers as the primary material and template. By carefully regulating the concentration of the iron nitrate impregnation solution, accurate loading of $Fe_3O_4$ nanoparticles onto the carbonized hemp fiber was achieved. Due to its unique porous structure, the balance between impedance matching, and electromagnetic loss, the prepared $Fe_3O_4$ nanoparticle/carbonized hemp fiber composite exhibits light weight, high absorption strength, and broadband absorption characteristics. The broadest absorption bandwidth of 6.1 GHz can be achieved, covering the entire Ku-band, and the minimum refection loss is as low as −49.7 dB. More interestingly, the Fe3O4 nanoparticle/carbonized hemp fiber composite exhibits attractive microwave absorption performance in both the X-band and Ku-band even with a wide range of $Fe_3O_4$ nanoparticle loading. Furthermore, simulations of the radar cross section (RCS) have confirmed that the $Fe_3O_4$ nanoparticle/carbonized hemp fiber composite is effective in attenuating electromagnetic waves in a real environment. This work presents an economical and efficient method for the development of porous carbon-based absorbents.
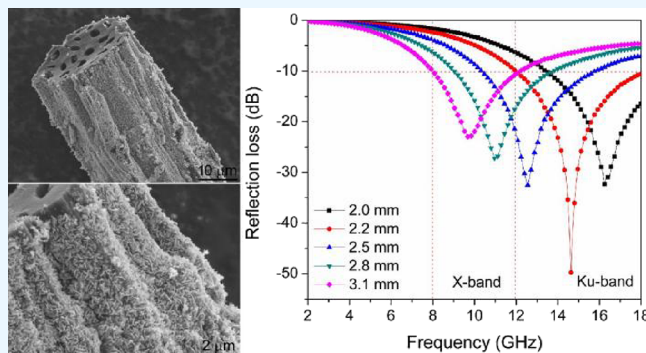
## 1. INTRODUCTION

The rapid development of wireless communication technology and intelligent device has brought great convenience to people's lives, but the electromagnetic radiation and interference generated can also affect people's production and life.[1,2] Additionally, the use of these technologies in military stealth applications has greatly increased the demand for research on microwave-absorbing materials. Therefore, developing microwave-absorbing materials with excellent comprehensive performance has significant research significance and practical application value in the field of electromagnetic protection.[3,4] Based on the loss mechanism of electromagnetic waves, traditional microwave-absorbing materials can be divided into two types: electrical loss type and magnetic loss type.[5,6] Electric loss materials have the advantage of high dielectric loss, but their high complex permittivity and nonmagnetic nature can cause poor impedance matching. Therefore, the combination of electric loss absorbent and magnetic loss absorbent to regulate electromagnetic parameters and enhance microwave absorption performance is of great practical significance.[7,8]

The absorption performance of a material not only depends on its composition but also is closely related to the overall structural design of the material.[9,10] Composite materials with core−shell, hollow, or three-dimensional porous characteristics contain abundant heterogeneous interfaces, which are conducive to electromagnetic energy attenuation.[11,12] Due to the excellent chemical stability, special microstructure, excellent conductivity, and low density, porous carbon materials have gradually become a popular research topic and application direction pursued by academia and industry in the field of microwave absorption.[13,14] Coating magnetic materials on the surface of porous carbon materials can effectively improve absorption performance, which is originated from the synergistic effect of the impedance matching and multiple electromagnetic loss mechanism.[15,16] Therefore, the development of inexpensive, readily available, high-strength, and broadband porous carbon-based composite microwave-absorbing materials has significant research value in terms of cost.

Natural plant fibers are mainly composed of cellulose and have unique microstructures and chemical components,

making them economically feasible raw materials for preparing porous carbon fibers.[17,18] If these fibers are used to create new microwave-absorbing materials while maintaining their fine morphology and structure, then their value will be greatly enhanced. Hemp fiber, derived from various hemp plants, is one of the most affordable natural fibers and is widely used in textiles and other industries. Jute fiber belongs to the category of hemp fiber, and its cross section is polygonal. The jute fiber contains several cavities in its center, which are circular or oval in shape. This unique structure allows for excellent moisture absorption and breathability.[19,20] Additionally, this characteristic makes jute fiber a cost-effective option for producing carbonized jute fibers with numerous macropores.[21,22] Furthermore, jute fibers have the advantage of being woven, making them practical for various applications. $Fe_3O_4$ is a commonly used magnetic absorbent due to its high complex permeability and magnetic loss, making it ideal for optimizing the microwave absorption performance of magnetic–dielectric composites.[23,24] Therefore, it is important to develop a simple and feasible synthesis process that effectively combines $Fe_3O_4$ nanoparticles with carbonized hemp fiber for microwave absorption using jute fiber as a carbon source.

In this paper, inexpensive and readily available natural jute fibers were used as a primary material to prepare carbonized hemp fibers with numerous macropores. Through a simple impregnation and calcination process, an $Fe_3O_4$ nanoparticle/carbonized hemp fiber ($Fe_3O_4$/CHF) composite was successfully prepared. Furthermore, the amount of $Fe_3O_4$ nanoparticles can be adjusted, resulting in improved impedance matching and multiple electromagnetic losses. This results in an excellent microwave absorption performance.

## 2. EXPERIMENTAL SECTION

**2.1. Materials.** $Fe(NO_3)_3 \cdot 9H_2O$ was procured from Tianjin Tianli Chemical Reagent Co., Ltd. The hemp fibers come from a commercially available jute rope with a 1 mm diameter.

**2.2. Preparation of the $Fe_3O_4$/CHF Composite.** The typical preparation process includes the following three steps.

1. A certain amount of hemp fibers was put into a tube furnace and calcined at 700 °C in a $N_2$ atmosphere for 2 h. The carbonized hemp fibers were obtained and denoted as CHF.

2. The carbonized hemp fibers were soaked in iron nitrate solutions for 24 h with concentrations of 0.1, 0.4, and 0.7 mol/L. Then, the soaked hemp fibers were picked out with tweezers and dried at 60 °C in a drying oven, loading iron nitrate onto carbonized hemp fibers.

3. The dried samples were first placed in a muffle furnace and calcined at 250 °C for 2 h, and iron oxide was loaded onto the carbonized hemp fibers. Subsequently, it was placed in a tube furnace and calcined at 550 °C for 2 h under a $N_2$ atmosphere, and $Fe_3O_4$/CHF composites were obtained through carbothermal reduction. To clarify, based on the concentration of iron nitrate solution (0.1, 0.4, and 0.7 mol/L), the products were named $Fe_3O_4$/CHF-0.1, $Fe_3O_4$/CHF-0.4, and $Fe_3O_4$/CHF-0.7, respectively.

**2.3. Characterization.** The structure and phase of the samples were characterized by X-ray diffraction (XRD) using a Shimadzu XRD-6100 powder X-ray diffractometer with Cu Kα radiation ($\lambda$ = 1.54 Å). The graphitization degree of carbon

was characterized through Raman spectroscopy with a Dxr2xi Raman spectrometer. A Thermo Scientific K-Alpha X-ray photoelectron spectrometer (XPS) was used to study the elemental composition. The morphology was obtained using a JSM-7001F scanning electron microscope (SEM) with an energy dispersive spectrometer (EDS). The BET special specific surface areas were determined by a nitrogen isothermal adsorption–desorption analyzer (Micromeritics ASAP 2460). The magnetic performance analysis was conducted using a Lake Shore7404 vibrating sample magnetometer (VSM) with a scanning range of −20 to 20 kOe. The content of magnetic components in the synthesized composite materials was obtained by using a PerkinElmer STA6000 synchronous thermal analyzer. To evaluate the microwave absorption performance, the sample was mixed with paraffin in a 1:1 mass ratio and then pressed into a coaxial ring shape for the coaxial-line method test. The electromagnetic parameters (complex permittivity $\varepsilon_r$ and complex permeability $\mu_r$) in the 2–18 GHz frequency range were measured using an Agilent N5244A vector network analyzer. Based on the measured $\varepsilon_r$ and $\mu_r$, the reflection loss (RL) of the material can be calculated according to the following formula:[25,26]

$$Z_{in} = \sqrt{\frac{\mu_r}{\varepsilon_r}} \tanh\left[ j\left(\frac{2\pi f d}{c}\right)\sqrt{\mu_r \varepsilon_r} \right] \tag{1}$$

$$RL(dB) = 20\log\left|\frac{Z_{in} - Z_0}{Z_{in} + Z_0}\right| \tag{2}$$

In the formula, $Z_{in}$ and $Z_0$ represent the input characteristic impedance of the absorbent and the characteristic impedance of free space, respectively; $c$ denotes the speed of light in free space; and $f$ and $d$ represent the frequency of electromagnetic waves and the thickness of the absorbent, respectively.

## 3. RESULTS AND DISCUSSION

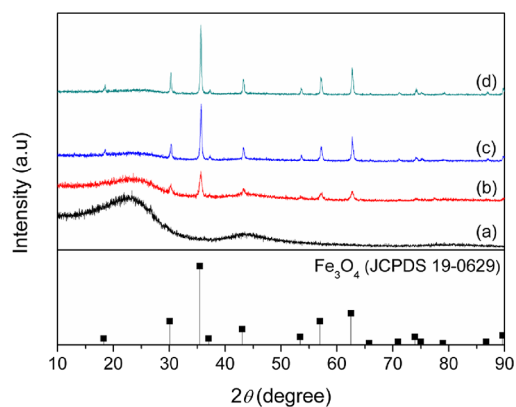**3.1. Phase and Morphology Analysis.** Figure 1a represents the XRD spectrum of carbonized hemp fibers, and



**Figure 1.** XRD patterns of CHF, $Fe_3O_4$/CHF-0.1, $Fe_3O_4$/CHF-0.4, and $Fe_3O_4$/CHF-0.7.

the broad peaks at 15−30 and 40−50° denote the diffraction peaks of amorphous carbon.[27,28] Figure 1b−d shows the XRD spectra of $Fe_3O_4$/CHF composites obtained using carbonized hemp fibers as carbon sources at different concentrations of iron nitrate. The narrow and sharp diffraction peaks in all spectra are consistent with $Fe_3O_4$ (JCPDS 19-0629), indicating good crystallinity.[29] Due to the thermal decomposition of iron
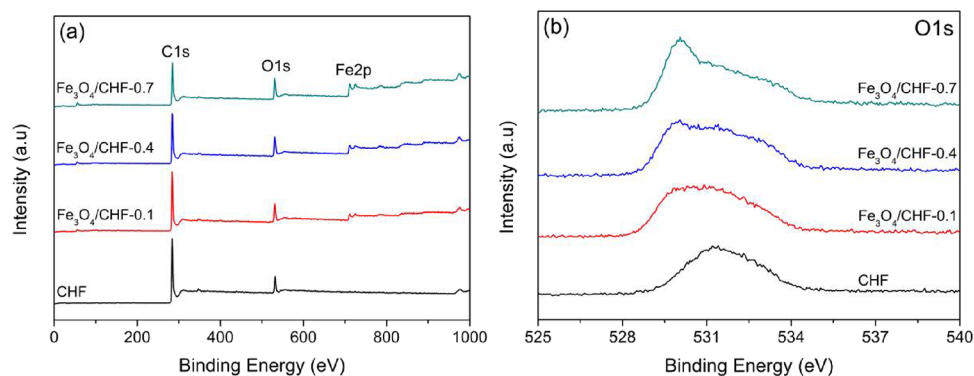
**Figure 2.** Wide-scan XPS spectra (a) and O 1s XPS spectra (b) of CHF, $Fe_3O_4$/CHF-0.1, $Fe_3O_4$/CHF-0.4, and $Fe_3O_4$/CHF-0.7.
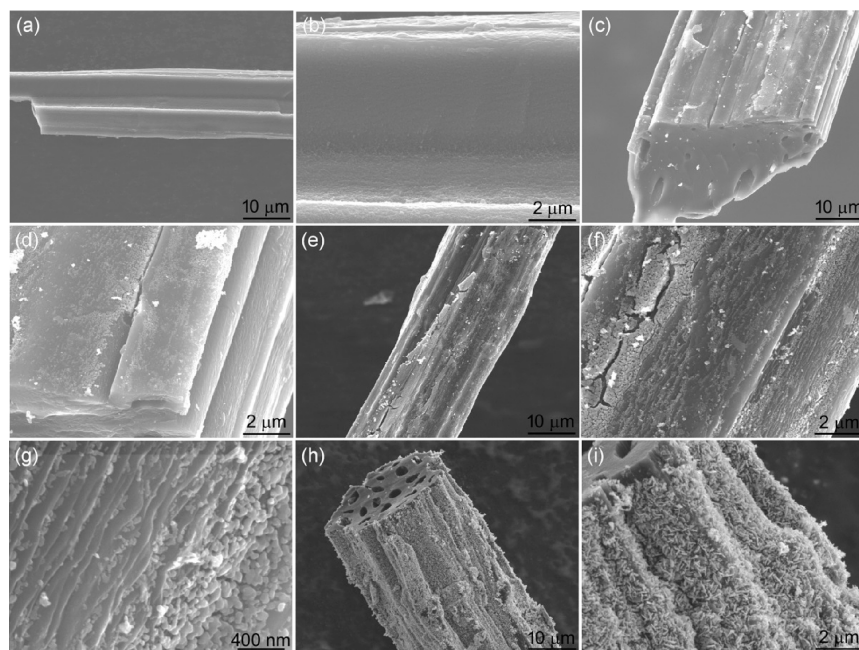


**Figure 3.** SEM images of the synthesized samples: (a and b) CHF, (c and d) $Fe_3O_4$/CHF-0.1, (e−g) $Fe_3O_4$/CHF-0.4, and (h and (i) $Fe_3O_4$/CHF-0.7.

nitrate, the generation of $Fe_3O_4$ occurs through the carbothermal reduction reaction in a $N_2$ atmosphere. As the concentration of iron nitrate increases, the diffraction peaks of $Fe_3O_4$ become more prominent, whereas the diffraction peaks of amorphous carbon weaken. The Raman spectra of CHF, $Fe_3O_4$/CHF-0.1, $Fe_3O_4$/CHF-0.4, and $Fe_3O_4$/CHF-0.7 are shown in Figure S2. All of these spectra exhibit two distinct peaks at approximately 1340 and 1590 cm$^{-1}$, which correspond to the D and G bands, respectively, in carbon components.[30] Furthermore, the intensity ratio of the D band to G band ($I_D$/$I_G$) is approximately 0.9 for these four samples, indicating that the loading of $Fe_3O_4$ does not change the graphitization degree of the carbonized hemp fibers.

XPS was utilized to measure the composition and valence states of CHF and $Fe_3O_4$/CHF composites, as depicted in Figure 2. The wide-scan XPS spectrum is shown in Figure 2a. For CHF, the XPS peaks of C 1s and O 1s are clearly visible at 284.5 and 531.5 eV, respectively. In addition, characteristic peaks of Fe 2p can be observed at 711.2 eV for the $Fe_3O_4$/CHF composites. As the $Fe_3O_4$ content increases, the intensity of the Fe 2p peak also increases. The XPS spectrum of the O 1s is shown in Figure 2b. As the $Fe_3O_4$ content increases, the

peak of O 1s shifts toward a lower binding energy, indicating a decrease in C═O and C−O bonds and an increase in the Fe−O bond.[31] These oxygen-containing groups can act as active sites for dipole polarization, thereby facilitating electromagnetic wave absorption.[32]

The SEM images of hemp fibers are displayed in Figure S2. The diameter of the hemp fibers ranges from 20 to 40 μm. Figure 3a,b indicates the SEM images of carbonized hemp fibers, and the diameter of the carbonized hemp fiber ranges from 20 to 40 μm. Figure 3c−i shows the SEM images of $Fe_3O_4$/CHF-0.1, $Fe_3O_4$/CHF-0.4, and $Fe_3O_4$/CHF-0.7, demonstrating the successful loading of $Fe_3O_4$ nanoparticles onto the porous carbonized hemp fibers. The amount of loaded $Fe_3O_4$ nanoparticles increases from $Fe_3O_4$/CHF-0.1 to $Fe_3O_4$/CHF-0.7, which is consistent with the XRD results. In $Fe_3O_4$/CHF-0.7, the $Fe_3O_4$ nanoparticles almost cover the carbonized hemp fibers, forming a coating structure. The photos of the CHF and $Fe_3O_4$/CHF-0.4 are displayed in Figures S3 and S4. The carbonized hemp fiber bundle with a 1 mm diameter is composed of multiple individual fibers. The low-magnification SEM images of carbonized hemp fibers are shown in Figure S5. Pores of various sizes can be discovered on the cross section,
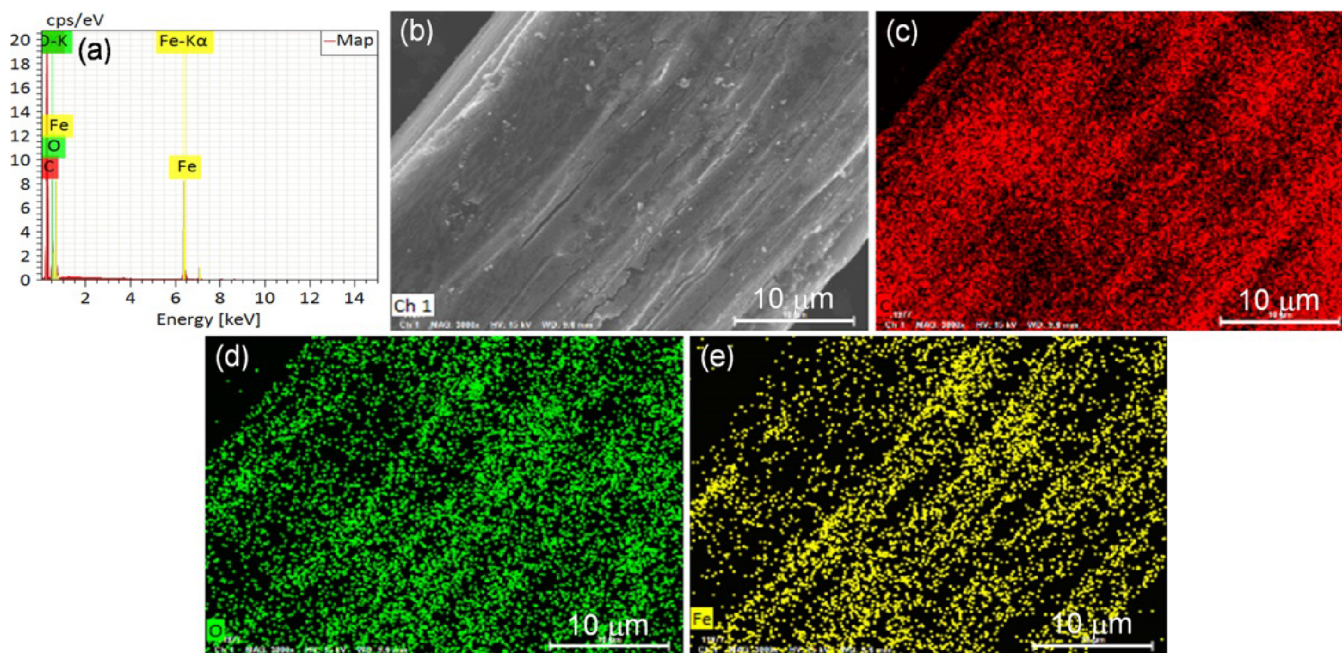
**Figure 4.** (a) EDS spectra and (b−e) elemental mapping images of $Fe_3O_4$/CHF-0.4.

which are originated from the original jute fibers.[21,22] Figure 4 shows the EDS element diagram and element mapping image of $Fe_3O_4$/CHF-0.4. The results indicate that the composite is primarily composed of C, Fe, and O elements, with O and Fe uniformly distributed along the carbonized hemp fibers in different colors, indicating a uniform loading of $Fe_3O_4$ nanoparticles on the carbonized hemp fiber. In summary, $Fe_3O_4$/CHF composites were successfully obtained using carbonized hemp fibers obtained from hemp fibers as carbon sources and templates. According to the calculation of the original $N_2$-adsorption data (Figure S6), the BET surface areas of CHF, $Fe_3O_4$/CHF-0.1, $Fe_3O_4$/CHF-0.4, and $Fe_3O_4$/CHF-0.7 are 276.46, 408.48, 410.94, and 380.69 $m^2/g$, respectively. This suggests that loading $Fe_3O_4$ nanoparticles promotes the formation of rich pore structures, but excessive loading can occupy some pores and decrease the specific surface area.

The thermogravimetric (TG) curve of hemp fiber is shown in Figure S7a. A distinct weight decrease is visible between 250 and 400 °C, which is attributed to the pyrolysis of hemp fibers into carbonized hemp fiber. After iron nitrate was loaded onto the carbonized hemp fibers and calcined at 250 °C for 2 h in a muffle furnace, iron oxide was loaded onto the carbonized hemp fibers. The TG curves of the $\alpha$-$Fe_2O_3$/CHF samples in a $N_2$ atmosphere are shown in Figure S7b. The distinct weight decrease is due to the removal of absorbed water and carbothermal reduction at high temperature. Figure 5 shows the TG curves of $Fe_3O_4$/CHF-0.1, $Fe_3O_4$/CHF-0.4, and $Fe_3O_4$/CHF-0.7 under an air atmosphere with a heating rate of 10 °C/min. The analysis reveals a significant weight loss due to the evaporation of adsorbed water and oxidation of carbon. The weight stabilizes at 607, 580, and 563 °C for $Fe_3O_4$/CHF-0.1, $Fe_3O_4$/CHF-0.4, and $Fe_3O_4$/CHF-0.7, respectively, and the decrease in stable temperature mainly comes from the decrease in carbon content. As carbon turns into gas and is removed in a high-temperature air atmosphere, the remaining product will only be $\alpha$-$Fe_2O_3$. The $Fe_3O_4$ content on the $Fe_3O_4$/CHF composite can be estimated using the following formula:[33]
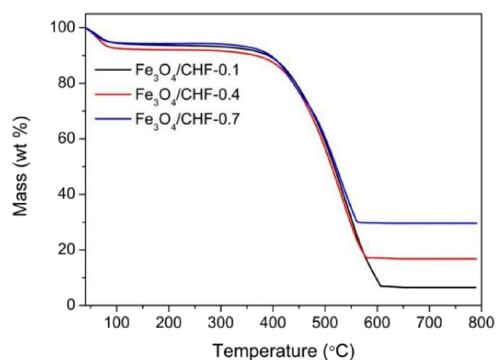


**Figure 5.** TG curves of $Fe_3O_4$/carbonized hemp fibers in an air atmosphere.

$$M(Fe_3O_4) = \frac{2 \times 232 \times R}{3 \times 160} \qquad (3)$$

where 160 is the molecular weight of $\alpha$-$Fe_2O_3$, 232 is the molecular weight of $Fe_3O_4$, $R$ is the percentage of residual mass, and $M$ stands for the $Fe_3O_4$ content on the $Fe_3O_4$/CHF composite. Based on the formula and TG curves, the weight percentage of $Fe_3O_4$ nanoparticles on $Fe_3O_4$/CHF-0.1, $Fe_3O_4$/CHF-0.4, and $Fe_3O_4$/CHF-0.7 is 6.26, 16.19, and 28.63 wt %, respectively.

The magnetic properties of the absorbent were associated with its ability to absorb an electromagnetic wave. To determine the magnetic properties of the $Fe_3O_4$/CHF composites, a VSM was used at room temperature. The results, shown in Figure 6, indicate that all samples exhibit typical ferromagnetism.[34] Specifically, the magnetic saturation (Ms) values of $Fe_3O_4$/CHF-0.1, $Fe_3O_4$/CHF-0.4, and $Fe_3O_4$/CHF-0.7 are 1.95, 7.99, and 19.59 emu/g, respectively. It can be observed that the Ms increases with increasing magnetic $Fe_3O_4$ content.

**3.2. Microwave Absorption Performance analysis.** The electromagnetic parameters are important indicators for evaluating the microwave absorption performance. Therefore,
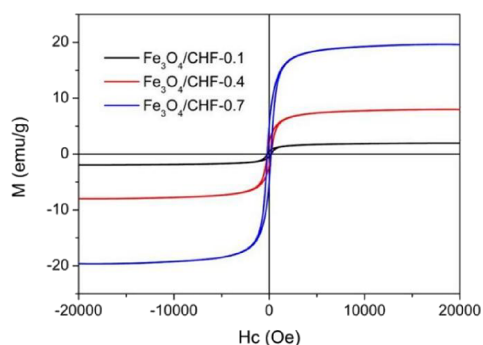
**Figure 6.** Hysteresis loops of $Fe_3O_4$/carbonized hemp fibers.

adjusting these parameters is the most direct and effective way to design microwave-absorbing materials. The complex permittivity ($\varepsilon_r = \varepsilon' - j\varepsilon''$) and complex permeability ($\mu_r = \mu' - j\mu''$) are the two most important electromagnetic parameters. $\varepsilon'$ and $\varepsilon''$ stand for the capacity and loss of electric field energy, respectively, while $\mu'$ and $\mu''$ indicate the storage and loss of magnetic energy, respectively.[35,36] Figure 7a shows the $\varepsilon'$ and $\varepsilon''$ of CHF, $Fe_3O_4$/CHF-0.1, $Fe_3O_4$/CHF-0.4, and $Fe_3O_4$/CHF-0.7 in the frequency range of 2−18 GHz. It can be observed that both $\varepsilon'$ and $\varepsilon''$ decrease as the frequency increases. According to the free electron theory, $\varepsilon'' = 1/(2\pi\rho f\varepsilon_0)$, where $\rho$ and $\varepsilon_0$ represent the electric resistivity and the permittivity of free space, respectively.[37,38] This indicates that the increase in the $Fe_3O_4$ content reduces the conductivity of the $Fe_3O_4$/CHF composite. Debye relaxation is typically

represented by the Cole−Cole curve, which can be expressed by the relationship between $\varepsilon'$ and $\varepsilon''$. Each semicircle on the curve of $\varepsilon'$ versus $\varepsilon''$ represents a Debye relaxation process.[39] The curves of $\varepsilon'$ versus $\varepsilon''$ for CHF, $Fe_3O_4$/CHF-0.1, $Fe_3O_4$/CHF-0.4, and $Fe_3O_4$/CHCF-0.7 are shown in Figure S8. All four samples exhibit two semicircles, indicating the presence of multiple relaxation processes, which are mainly attributed to the interface polarization and dipole polarization.[40] Interface polarization is primarily caused by a large number of interfaces, resulting from the unique microstructure of the material. On the other hand, dipole polarization is primarily related to defects within the material. Both of these processes contribute to the improvement of the material's microwave absorption performance. Additionally, it can be observed that in the high complex permittivity region, the curves of $\varepsilon'$ versus $\varepsilon''$ show a linear increase, which is attributed to the high conductivity of CHF.

Figure 7b shows the $\mu'$ and $\mu''$ in the frequency range of 2−18 GHz. The $\mu''$ value of CHF is approximately 0, but it increases with the increase of the $Fe_3O_4$ amount, indicating an increase in magnetic loss. In general, the magnetic loss in the 2−18 GHz range is mainly due to natural resonance, exchange resonance, and eddy current loss. Eddy current loss can be analyzed using $\mu'' \approx 2\pi\mu_0(\mu')^2\sigma d^2 f/3$, where $\mu_0$, $\sigma$, and $d$ represent the permeability in a vacuum, electrical conductivity, and size of particles, respectively.[41] If the magnetic loss only comes from eddy current loss, the value of $C_0$ ($C_0 = \mu''(\mu')^{-2}f^{-1} = 2\pi\mu_0\sigma d^2/3$) should remain constant as the frequency varies.[42] Figure 7c shows the curves of $C_0$ versus $f$ for
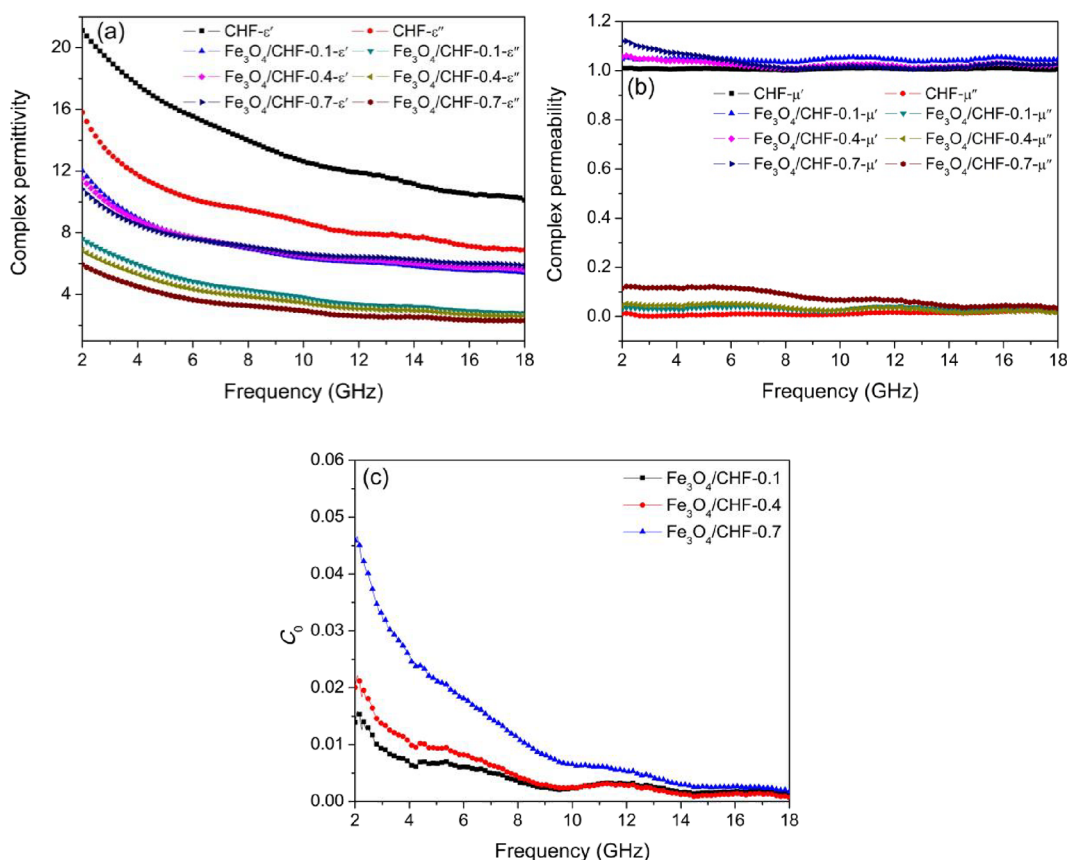


**Figure 7.** (a) Complex permittivity; (b) complex permeability for CHF, $Fe_3O_4$/CHF-0.1, $Fe_3O_4$/CHF-0.4, and $Fe_3O_4$/CHF-0.7; and (c) curves of $C_0$ versus $f$ for $Fe_3O_4$/CHF-0.1, $Fe_3O_4$/CHF-0.4, and $Fe_3O_4$/CHF-0.7.
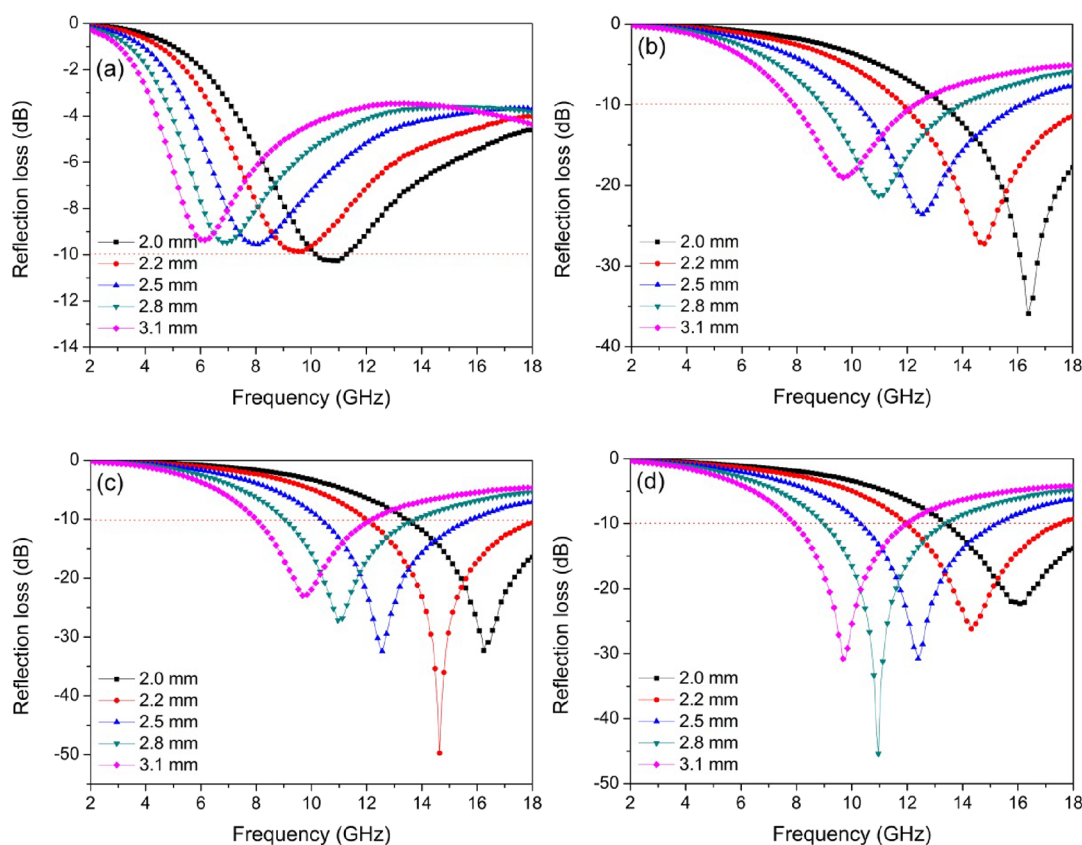
**Figure 8.** RL curves of (a) CHF, (b) Fe$_3$O$_4$/CHF-0.1, (c) Fe$_3$O$_4$/CHF-0.4, and (d) Fe$_3$O$_4$/CHF-0.7 at different thicknesses.

Fe$_3$O$_4$/CHF-0.1, Fe$_3$O$_4$/CHF-0.4, and Fe$_3$O$_4$/CHF-0.7, which have three fluctuations in the range of 4−9, 10−14, and 14−18 GHz. This suggests that the magnetic loss mainly comes from the natural resonance and exchange resonance, and the resonance peaks at relatively low frequencies are caused by natural resonance, whereas those at higher frequencies result from exchange resonance.[43]

Figure 8 displays the RL curves of CHF, Fe$_3$O$_4$/CHF-0.1, Fe$_3$O$_4$/CHF-0.4, and Fe$_3$O$_4$/CHF-0.7. It is important to note that the thickness of the samples affects their microwave absorption, and the absorption value shifts toward the low-frequency region as the thickness increases. According to the $\lambda/4$ theory, the thickness ($t$) of the absorbent follows the following formula: $t_m = n\lambda_0/4(|\mu_r||\varepsilon_r|)^{1/2} = nc/4f_m(|\mu_r||\varepsilon_r|)^{1/2}$ ($n$ = 1, 3, 5, ...).[44,45] In this formula, $t_m$ and $\lambda_0$ represent the matching thickness of the absorbent and the wavelength of electromagnetic waves, respectively. It is clear that the matching thickness is inversely proportional to the frequency on the RL curves, and the thickness can be adjusted to regulate the RL value and the position of the reflection peak according to specific needs. Additionally, when $t_m$ of the absorbent follows the $\lambda/4$ model, the input impedance is equal to the air wave impedance, resulting in a minimum RL value. Simulation and calculation of $t_m$ versus $f_m$ for these four samples are shown in Figure S9, and it is obvious that the calculated results are in good agreement with the simulated values. For CHF, the effective bandwidth is 1 GHz (10.2−11.2 GHz) with a minimum RL of −10.3 dB at a thickness of 2 mm. For Fe$_3$O$_4$/CHF-0.1, the effective bandwidth is 6.1 GHz (11.9−18 GHz) at a thickness of 2.2 mm, covering the entire Ku-band (12−18 GHz). For Fe$_3$O$_4$/CHF-0.4, the minimum RL reaches −49.7 dB at a thickness of 2.2 mm, and the effective bandwidth is 6

GHz (12−18 GHz). For Fe$_3$O$_4$/CHF-0.7, the effective bandwidth is 5.5 GHz (12−17.5 GHz) at a thickness of 2.2 mm. Interestingly, for Fe$_3$O$_4$/CHF-0.1, Fe$_3$O$_4$/CHF-0.4, and Fe$_3$O$_4$/CHF-0.7, the effective bandwidth covers the entire X-band (8−12 GHz) at a thickness of 3.1 mm. Furthermore, at a matching thickness of 2.2 mm, the combination of carbonized hemp fiber and Fe$_3$O$_4$ can improve microwave absorption performance, but excessive Fe$_3$O$_4$ content will lead to a decrease in microwave absorption performance. For the magnetic−dielectric composite, the amount of magnetic component must be appropriate. Overall, the Fe$_3$O$_4$/CHF composites possess excellent microwave absorption performance in both the X-band and Ku-band for different Fe$_3$O$_4$ contents, making them promising materials for various applications. Table 1 displays a selection of porous carbon-based microwave absorbents, while a comparison of their microwave absorption performance with our work can be found in Figure S10. It is evident that the Fe$_3$O$_4$/CHF composites have wider effective bandwidth and stronger microwave absorption.[46−53] Furthermore, compared to traditional magnetic microwave absorbents, the Fe$_3$O$_4$/CHF composites possess the benefits of being lightweight and cost-effective, which are attributed to the inclusion of carbonized hemp fibers. This abundant natural source and simple preparation method make the Fe$_3$O$_4$/CHF composite a cost-effective, lightweight, and broadband microwave absorbent with great potential for various applications.

Generally speaking, the excellent microwave absorption capability of a material can be attributed to the synergistic effect of its impedance matching characteristics and attenuation characteristics.[54,55] Good impedance matching can reduce the reflection of electromagnetic waves on the surface

**Table 1. Microwave Absorption Performances of Some Reported Porous Carbon-Based Absorbents**

| sample | effective absorption bandwidth (GHz) | minimum RL (dB) | refs |
|---|---|---|---|
| porous carbon/Fe$_3$O$_4$@Fe | 5.0 | −49.6 | 46 |
| PANI/biomass derived porous carbon | 4.2 | −40.9 | 47 |
| FeCo/bamboo derived carbon | 4.7 | −40.0 | 48 |
| Fe@porous carbon@ carbon fiber | 5.2 | −46.2 | 49 |
| cotton fiber derived RGO/ Ni/C composite | 4.6 | −39.3 | 50 |
| ferrite/Co/porous carbon | 4.8 | −31.0 | 51 |
| hollow core−shell CoNi@ C composites | 5.0 | −35.8 | 52 |
| porous Fe$_3$O$_4$/carbon fiber | 5.1 | −48.2 | 53 |
| Fe$_3$O$_4$/CHF composites | 6.1 | −49.7 | this work |

of the absorbent, allowing for maximum incidence into the interior of the absorbent. When the impedance matching coefficient (Z) is close to 1, the majority of incident electromagnetic waves can penetrate the surface of a material with minimal microwave reflection. On the other hand, impedance mismatch (a large difference between $Z_{in}$ and $Z_0$) can cause the incident electromagnetic wave to reflect off the surface of the absorbent. This renders the internal loss mechanism ineffective, resulting in poor absorption performance.[56] The Z can be calculated using the following formula:[57,58]

$$Z = \left| \frac{Z_{in}}{Z_0} \right| = \sqrt{\frac{\mu_r}{\varepsilon_r}} = \sqrt{\frac{\sqrt{\mu''^2 + \mu'^2}}{\sqrt{\varepsilon''^2 + \varepsilon'^2}}} \tag{4}$$

Dielectric loss and magnetic loss are two crucial factors that contribute to microwave attenuation, expressed as $\tan \delta_e = \varepsilon''/\varepsilon'$ and $\tan \delta_m = \mu''/\mu'$, respectively. Generally, higher $\tan \delta_e$ and $\tan \delta_m$ values indicate greater absorption of electromagnetic waves. Therefore, efficient microwave absorption relies on the combined effect of dielectric loss and magnetic loss. Figure 9a shows the $\tan \delta_e$ and $\tan \delta_m$ values for CHF, Fe$_3$O$_4$/CHF-0.1, Fe$_3$O$_4$/CHF-0.4, and Fe$_3$O$_4$/CHF-0.7. The $\tan \delta_e$ is greater than the $\tan \delta_m$, indicating that dielectric loss plays a more significant role. Dielectric loss is primarily caused by two factors: conductivity loss and polarization loss.[59] Conductivity loss occurs when conductive charge carriers, such

as ions or electrons, are present within the dielectric material. This is directly linked to the material's conductivity. The high conductivity of carbonized hemp fiber results in the highest $\tan \delta_e$ value, which decreases as the amount of Fe$_3$O$_4$ increases. This is because the carbonized hemp fiber forms a conductive network, enhancing conductivity loss. The polarization loss is related to the polarization characteristics of materials, primarily resulting from the interface polarization and dipole polarization. This has been illustrated in Figure S8. Additionally, the $\tan \delta_m$ values increase significantly with the increase in Fe$_3$O$_4$ content due to the magnetism of Fe$_3$O$_4$.

Figure 9b shows the impedance matching coefficients for CHF, Fe$_3$O$_4$/CHF-0.1, Fe$_3$O$_4$/CHF-0.4, and Fe$_3$O$_4$/CHF-0.7. The low Z value of CHF indicates an impedance mismatch, which is attributed to the high conductivity of carbonized hemp fibers, ultimately leading to poor microwave absorption performance. However, for Fe$_3$O$_4$/CHF-0.1, Fe$_3$O$_4$/CHF-0.4, and Fe$_3$O$_4$/CHF-0.7, the Z values are much higher, indicating excellent impedance matching. Furthermore, the Z value increases with frequency, which is beneficial for high-frequency microwave absorption. Additionally, as the Fe$_3$O$_4$ content increases, the Z value decreases in the high-frequency range and increases in the low-frequency range. This feature allows for the regulation of the absorption frequency band by controlling the Fe$_3$O$_4$ content. However, excessive Fe$_3$O$_4$ content will lead to a decrease in microwave absorption performance due to low dielectric loss. In brief, for an absorbent dominated by dielectric loss, the amount of magnetic component must be appropriate, taking into account the effects of impedance matching and electromagnetic loss.

Based on the discussion above, the microwave absorption mechanism for the Fe$_3$O$_4$/CHF composite can be summarized in Figure 10. First, loading Fe$_3$O$_4$ nanoparticles onto the carbonized hemp fibers improves impedance matching, allowing for a greater fraction of incoming electromagnetic waves to penetrate the air−absorbent interface. Additionally, the presence of Fe$_3$O$_4$ nanoparticles leads to a natural resonance and exchange resonance, contributing to magnetic energy loss. Second, the composite material forms a conductive network, which promotes conductive loss through electron migration and hopping. As the incident electromagnetic wave travels through this resistive conductive network, the induced microcurrent quickly weakens and transforms into thermal energy, resulting in the attenuation of the electromagnetic energy. Third, the numerous coexisting macropores in the carbonized hemp fibers promote multiple reflection and
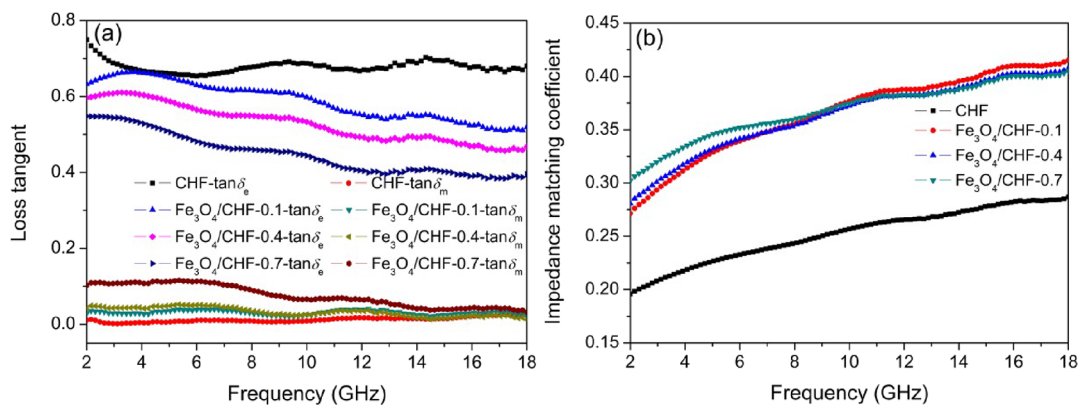
**Figure 9.** (a) Loss tangent and (b) impedance matching coefficient of CHF, Fe$_3$O$_4$/CHF-0.1, Fe$_3$O$_4$/CHF-0.4, and Fe$_3$O$_4$/CHF-0.7.
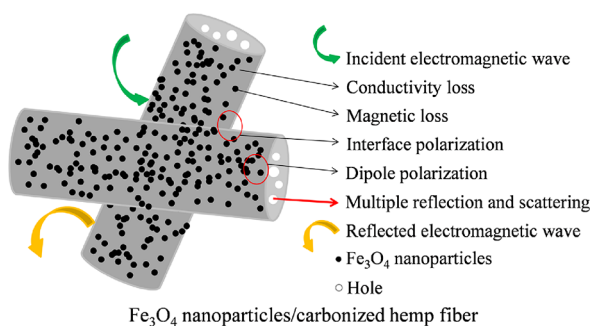
**Figure 10.** Possible microwave absorption mechanisms for the $Fe_3O_4$ nanoparticle/carbonized hemp fiber composite.

scattering of electromagnetic waves, aiding in energy attenuation.[60] Lastly, the different phase boundaries in the $Fe_3O_4$/CHF composite can accumulate the charges, inducing interface polarization.[61] Additionally, the defects from the carbothermal reduction act as dipole centers, leading to dipole polarization.[62] Both of these polarization processes contribute to the attenuation of the incident electromagnetic waves.

**3.3. Radar Cross-Section Simulation.** The radar cross section (RCS) is a crucial factor in evaluating the effectiveness of absorbent coatings on targets in real-world scenarios, and a lower RCS value denotes better absorption performance of the material.[63,64] In this study, CST simulation software was used to create a model of a perfect electrical conductor (PEC) substrate that can be used to simulate wave absorption material coverage. The $Z$ axis of the model represents the incident direction of the electromagnetic wave, whereas $\theta$ is used as the detection angle. The thickness of the PEC is set to 1 mm, whereas the absorbing coating is set to 2.2 mm. The simulation frequency is 14.64 GHz, which corresponds to the minimum

RL of $Fe_3O_4$/CHF-0.4. The RCS value was calculated using the following formula:[65,66]

$$RSC \, (dB \, m^2) = 10\log(\frac{4\pi S}{\lambda^2}|\frac{E_S}{E_i}|)^2 \tag{5}$$

where $S$ represents the area of the simulation plate, $\lambda$ denotes the wavelength of the incident electromagnetic wave, and $E_S$ and $E_i$ stand for the electric field strengths of the scattered wave and the incident waves, respectively.

Figure 11a−e shows the 3D simulation images of PEC, CHF-covered PEC, and $Fe_3O_4$/CHF composite-covered PEC, respectively. These images demonstrate that the PEC plane cannot absorb electromagnetic waves. The PEC covered by CHF also exhibits strong reflected waves, whereas the PEC coated with $Fe_3O_4$/CHF composites shows a significant reduction in reflected waves, indicating its ability to dissipate more electromagnetic wave energy under the same conditions. Figure 11f shows the curve of the RCS values with the detection angles ranging from −60 to 60°. The results indicate that the RCS values of the $Fe_3O_4$/CHF composites are much lower than those of the pure PEC model and CHF coating. The RCS values are consistently below −27.6 dB m² throughout the entire range, with the lowest value reaching −63.6 dB m². This suggests that the $Fe_3O_4$/CHF composites have an excellent radar wave attenuation ability as a coating material at all angles of incident waves. Furthermore, the simulation results align with the measured electromagnetic wave attenuation performance, indicating the practical application potential of $Fe_3O_4$/CHF composites in engineering. Figure S11 displays simulation curves of RCS values for $Fe_3O_4$/CHF-0.4 at various frequencies. These results demonstrate that the radar wave attenuation ability changes at different frequencies even with the same coating thickness of 2.2 mm. The thickness and frequency of the coating directly
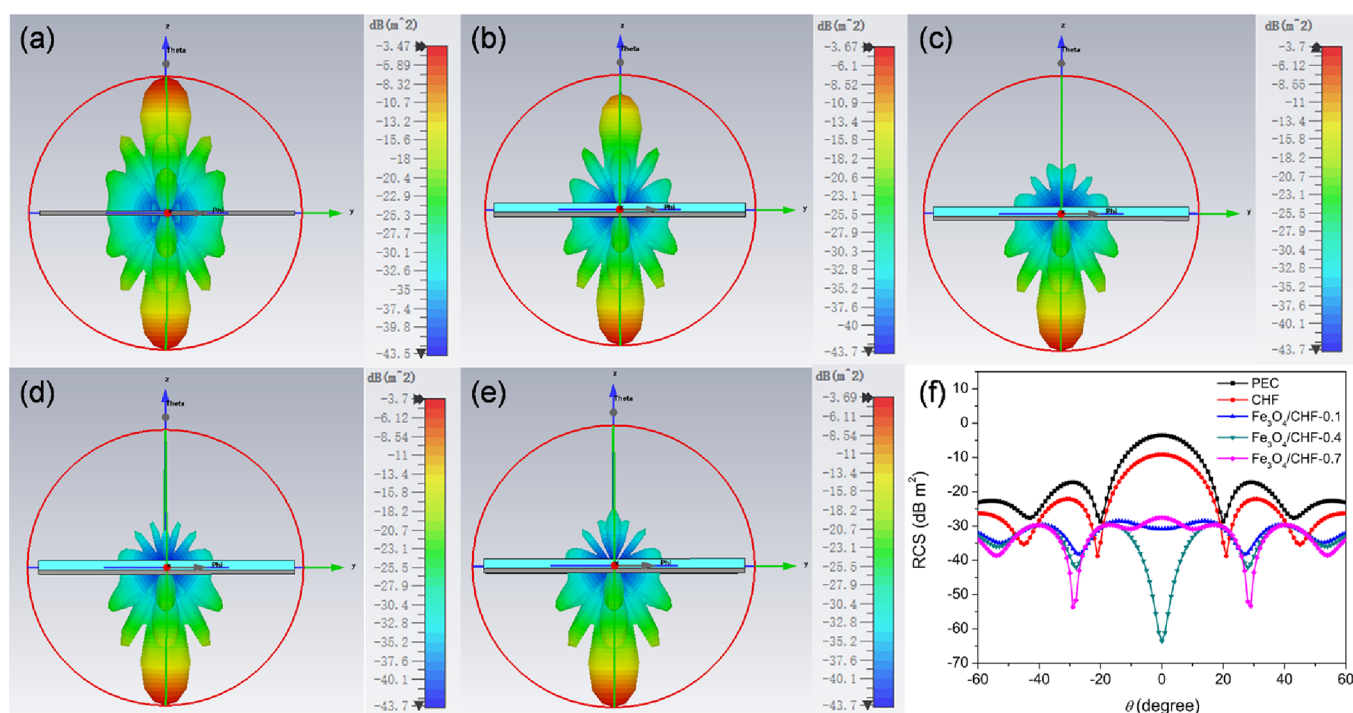


**Figure 11.** CST far-field simulation of (a) PEC and (b−e) CHF, $Fe_3O_4$/CHF-0.1, $Fe_3O_4$/CHF-0.4, and $Fe_3O_4$/CHF-0.7 cover PEC. (f) Simulation curves of RCS values for PEC, CHF, $Fe_3O_4$/CHF-0.1, $Fe_3O_4$/CHF-0.4, and $Fe_3O_4$/CHF-0.7 at different detection angles.

affect its radar wave attenuation ability. In the high-frequency range, the $Fe_3O_4$/CHF composite exhibits superior radar wave attenuation ability, which agrees well with the RL curves shown in Figure 8. In practical applications, the appropriate coating thickness should be chosen based on specific usage needs.

## 4. CONCLUSIONS

$Fe_3O_4$ nanoparticle/carbonized hemp fiber composites were successfully prepared using inexpensive and renewable hemp fibers as carbon sources and templates through a simple impregnation and calcination process. Moreover, the precise loading of $Fe_3O_4$ nanoparticles on carbonized hemp fiber can be achieved. Within a wide range of $Fe_3O_4$ loading, the $Fe_3O_4$ nanoparticle/carbonized hemp fiber composites possess excellent microwave absorption performance in both the X-band and Ku-band. Additionally, the RCS simulation results demonstrate that the combination of $Fe_3O_4$ nanoparticles and carbonized hemp fibers shows promising potential for practical use. This work provides a green, simple, and efficient method for preparing low-cost, lightweight, and broadband microwave-absorbing materials.

## ASSOCIATED CONTENT

### Supporting Information

The Supporting Information is available free of charge at https://pubs.acs.org/doi/10.1021/acsomega.4c07063.

> The Raman spectra, original $N_2$-adsorption data plot, curves of $\varepsilon'$ versus $\varepsilon''$, and curves of the absorbent thickness ($t_m$) versus peak frequency ($f_m$) for CHF, $Fe_3O_4$/CHF-0.1, $Fe_3O_4$/CHF-0.4, and $Fe_3O_4$/CHF-0.7; the photos of the hemp fiber, CHF, and $Fe_3O_4$/CHF-0.4; the TG curves of hemp fibers and $\alpha$-$Fe_2O_3$/carbonized hemp fibers in a $N_2$ atmosphere; comparison of microwave absorption performance with recently reported porous carbon-based absorbents; and the simulation curves of RCS values for $Fe_3O_4$/CHF-0.4 at different frequencies (PDF)

## AUTHOR INFORMATION

### Corresponding Authors

**Wanxi Li** − *Department of Materials Science and Engineering, Jinzhong University, Jinzhong 030619, P. R. China;* orcid.org/0000-0001-8100-8247; Email: liwanxi1986@163.com

**Yali Zhao** − *Department of Materials Science and Engineering, Jinzhong University, Jinzhong 030619, P. R. China;* Email: yaliz12@163.com

### Authors

**Boqiong Li** − *Department of Materials Science and Engineering, Jinzhong University, Jinzhong 030619, P. R. China*

**Yingfen Wang** − *AVIC Composite Corporation Ltd., Beijing 101300, P. R. China*

**Hengliang Liang** − *AVIC Manufacturing Technology Institute, Beijing 101300, P. R. China*

**Baoliang Lv** − *School of Chemistry and Materials Science, Shanxi Normal University, Taiyuan 030031, P. R. China;* orcid.org/0000-0001-8288-6076

Complete contact information is available at:
https://pubs.acs.org/10.1021/acsomega.4c07063

### Author Contributions

Wanxi Li: Conceptualization, Data curation, Formal analysis, Writing−original draft, Writing−review and editing. Boqiong Li: Visualization. Yali Zhao: Methodology, Supervision. Yingfen Wang: Investigation. Hengliang Liang: Resources. Baoliang Lv: Validation.

### Notes

The authors declare no competing financial interest.

## ACKNOWLEDGMENTS

## REFERENCES

(1) Lv, H.; Yang, Z.; Xu, H.; Wang, L.; Wu, R. An electrical switch-driven flexible EM absorber. *Adv. Funct. Mater.* **2020**, *30*, No. 1907251.

(2) Xie, A. M.; Lin, X. P.; Zhang, C.; Cheng, S. Y.; Dong, W.; Wu, F. Oxygen vacancy mediated polymerization of pyrrole on $MoO_3$ to construct dielectric nanocomposites for EM waves absorption application. *J. Alloys Compd.* **2023**, *938*, No. 168523.

(3) Zhang, W. H.; Li, K.; Han, L. W.; Wu, T. Y.; Zhang, J. Y.; Cheng, J. Ultra-strength polyurethane/MOF-derived composites with self-healing and recycling capabilities and highly efficient microwave absorption properties. *J. Mater. Chem. C* **2024**, *12*, 1446−1458.

(4) Liu, P. B.; Zhu, C. Y.; Gao, S.; Guan, C.; Huang, Y.; He, W. J. N-doped porous carbon nanoplates embedded with $CoS_2$ vertically anchored on carbon cloths for flexible and ultrahigh microwave absorption. *Carbon* **2020**, *163*, 348−359.

(5) Yan, J.; Wang, Y.; Liu, W. J.; Liu, P. B.; Chen, W. X. Two-dimensional metal organic framework derived nitrogen-doped graphene-like carbon nanomesh toward efficient electromagnetic wave absorption. *J. Colloid Interface Sci.* **2023**, *643*, 318−327.

(6) Li, Y. J.; Yuan, M. W.; Liu, H. H.; Sun, G. B. Assembly of CoNi nanoparticles on Ketjenblack carbon with superior performance and optimized impedance matching for electromagnetic wave absorption. *J. Alloy. Compd.* **2019**, *798*, 790−799.

(7) Zhu, T.; Chang, S. C.; Song, Y. F.; Lahoubi, M.; Wang, W. PVP-encapsulated $CoFe_2O_4$/rGO composites with controllable EM wave absorption performance. *Chem. Eng. J.* **2019**, *373*, 755−766.

(8) Fan, G. H.; Jiang, Y. L.; Xin, J. H.; Zhang, Z. D.; Fu, X. Y.; Xie, P. T.; Cheng, C. B.; Liu, Y.; Qu, Y. P.; Sun, K.; Fan, R. H. Facile synthesis of $Fe@Fe_3C$/C nanocomposites derived from bulrush for excellent EM wave-absorbing properties. *ACS Sustain. Chem. Eng.* **2019**, *7*, 18765−18774.

(9) Wang, Y. H.; Han, X. J.; Xu, P.; Liu, D. W.; Cui, L. R.; Zhao, H. H.; Du, Y. C. Synthesis of pomegranate-like $Mo_2C@C$ nanospheres for highly efficient microwave absorption. *Chem. Eng. J.* **2019**, *372*, 312−320.

(10) Chen, L.; Sui, J.; Waterhouse, G. I. N.; Zhang, Z. M.; Yu, L. M. $Fe_{0.64}Ni_{0.36}@C$ and $Mo_2C@C$ and $Mo_2C@C$ heterostructures embedded in N−doped carbons as microwave absorbers. *J. Alloys Compd.* **2023**, *960*, No. 170820.

(11) Jiang, T.; Wang, Z. D.; Luo, Z. T.; He, J. H.; Hu, C. C.; Xiang, X. Y.; Cao, Y. F.; Fang, G.; Peng, K. S.; Liu, C. Y. Constructing heterogeneous conductive network with core-shell $Ag@Fe_3O_4$ for dual-band effective microwave absorption. *Appl. Surf. Sci.* **2023**, *610*, No. 155231.

(12) Liu, Y.; Wang, Y. H.; Ding, C. L.; Wang, Y. K.; Chen, Z. S.; Li, Z. G.; Lv, X. Y.; Shi, J. M.; Zhang, X. Research progress of transition metal carbide-based composites for microwave absorption. *J. Alloy. Compd.* **2024**, *1002*, No. 175381.

(13) Zhao, H. Q.; Jin, C. Q.; Yang, X.; Lu, P.; Cheng, Y. Synthesis of a one-dimensional carbon nanotube-decorated three-dimensional crucifix carbon architecture embedded with Co$_7$Fe$_3$/Co$_{5.47}$N nanoparticles for high-performance microwave absorption. *J. Colloid Interface Sci.* **2023**, *645*, 22−32.

(14) Wu, Z.; Yao, C.; Meng, Z.; Deng, Y.; Wang, Y.; Liu, J.; Wang, Y.; Zhou, H. Biomass-derived crocodile skin-like porous carbon for high-performance microwave absorption. *Adv. Sustainability Syst.* **2022**, *6*, No. 2100454.

(15) Zhao, H. Q.; Cheng, Y.; Zhang, Z.; Yu, J. W.; Zheng, J.; Zhou, M.; Zhou, L.; Zhang, B. S.; Ji, G. B. Rational design of core-shell Co@C nanotubes towards lightweight and highefficiency microwave absorption. *Composites Part B: Engineering* **2020**, *196*, No. 108119.

(16) Zhang, M. M.; Jiang, Z. Y.; Si, H. X.; Zhang, X. F.; Liu, C. X.; Gong, C. H.; Zhang, Y. H.; Zhang, J. W. Heterogeneous iron-nickel compounds/RGO composites with tunable microwave absorption frequency and ultralow filler loading. *Phys. Chem. Chem. Phys.* **2020**, *22*, 8639−8646.

(17) Guan, H. T.; Wang, Q. Y.; Wu, X. F.; Pang, J.; Jiang, Z. Y.; Chen, G.; Dong, C. J.; Wang, L. H.; Gong, C. H. Biomass derived porous carbon (BPC) and their composites as lightweight and efficient microwave absorption materials. *Composites Part B* **2021**, *207*, No. 108562.

(18) Long, A. C.; Zhao, P. F.; Liao, L. S.; Wang, R.; Tao, J. L.; Liao, J. H.; Liao, X. X.; Zhao, Y. F. Sustainable kapok fiber-derived carbon microtube as broadband microwave absorbing material. *Materials* **2022**, *15*, 4845.

(19) Wang, W. M.; Cai, Z. S.; Yu, J. Y.; Xia, Z. P. Changes in composition, structure, and properties of jute fibers after chemical treatments. *Fibers Polym.* **2009**, *10*, 776−780.

(20) Sambandamoorthy, S.; Narayanan, V.; Chinnapandi, L. B. M.; Aziz, A. Impact of fiber length and surface modification on the acoustic behaviour of jute fiber. *Appl. Acoust.* **2021**, *173*, No. 107677.

(21) Cho, D.; Kim, J. M.; Song, I. S.; Hong, I. Effect of alkali pretreatment of jute on the formation of jute-based carbon fibers. *Mater. Lett.* **2011**, *65*, 1492−1494.

(22) Wu, H.; Fan, S. W.; Yuan, X. W.; Chen, L. F.; Deng, J. L. Fabrication of carbon fibers from jute fibers by pre-oxidation and carbonization. *New Carbon Mater.* **2013**, *28*, 448−453.

(23) Wu, H. J.; Liu, J. L.; Liang, H. S.; Zang, D. Y. Sandwich-like Fe$_3$O$_4$/Fe$_3$S$_4$ composites for EM wave absorption. *Chem. Eng. J.* **2020**, *393*, No. 124743.

(24) Shu, X. F.; Zhou, J.; Lian, W.; Jiang, Y.; Wang, Y. Q.; Shu, R. W.; Liu, Y.; Han, J. J.; Zhuang, Y. Size-morphology control, surface reaction mechanism and excellent wave absorption characteristics of Fe$_3$O$_4$ hollow spheres. *J. Alloy. Compd.* **2021**, *854*, No. 157087.

(25) Liu, P. B.; Gao, S.; Liu, X. D.; Huang, Y.; He, W. J.; Li, Y. T. Rational construction of hierarchical hollow CuS@CoS$_2$ nanoboxes with heterogeneous interfaces for high-efficiency microwave absorption materials. *Compos. Part B Eng.* **2020**, *192*, No. 107992.

(26) Qin, M.; Zhang, L.; Zhao, X.; Wu, H. Defect induced polarization loss in multi-shelled spinel hollow spheres for electromagnetic wave absorption application. *Adv. Sci.* **2021**, *8*, No. 2004640.

(27) Liang, X. H.; Quan, B.; Chen, J. B.; Gu, W. H.; Zhang, B. S.; Ji, G. B. Nano bimetallic@carbon layer on porous carbon nanofibers with multiple interfaces for microwave absorption applications. *ACS Appl. Nano Mater.* **2018**, *1*, 5712−5721.

(28) Li, W. X.; Guo, F.; Zhao, Y. L.; Liu, Y. Y. A sustainable and low-cost route to design NiFe$_2$O$_4$ nanoparticles/biomass-based carbon fibers with broadband microwave absorption. *Nanomaterials* **2022**, *12*, 4063.

(29) Cheng, Y.; Cao, J. M.; Li, Y.; Li, Z. Y.; Zhao, H. Q.; Ji, G. B.; Du, Y. W. The outside-in approach to construct Fe$_3$O$_4$ nanocrystals/mesoporous carbon hollow spheres core-shell hybrids toward microwave absorption. *ACS Sustain. Chem. Eng.* **2018**, *6*, 1427−1435.

(30) Lian, Y.; Han, B.; Liu, D.; Wang, Y.; Zhao, H.; Xu, P.; Han, X.; Du, Y. Solvent-free synthesis of ultrafine tungsten carbide nanoparticles-decorated carbon nanosheets for microwave absorption. *Nano-Micro Lett.* **2020**, *12*, 153.

(31) Zhang, Q. C.; Du, Z. J.; Huang, X. Z.; Zhao, Z. X.; Guo, T.; Zeng, G. J.; Yu, Y. T. Tunable microwave absorptivity in reduced graphene oxide functionalized with Fe$_3$O$_4$ nanorods. *Appl. Surf. Sci.* **2019**, *473*, 706−714.

(32) Wang, C.; Han, X.; Xu, P.; Zhang, X.; Du, Y.; Hu, S.; Wang, J.; Wang, X. The electromagnetic property of chemically reduced graphene oxide and its application as microwave absorbing material. *Appl. Phys. Lett.* **2011**, *98*, No. 072906.

(33) Cheng, Y.; Seow, J. Z. Y.; Zhao, H.; Xu, Z. J.; Ji, G. A flexible and lightweight biomass-reinforced microwave absorber. *Nano-Micro Lett.* **2020**, *12*, 125.

(34) Yuan, J. S.; Zhang, Y.; Zhang, X. Y.; Zhao, L.; Shen, H. L.; Zhang, S. G. Template-free synthesis of core−shell Fe$_3$O$_4$@MoS$_2$@mesoporous TiO$_2$ magnetic photocatalyst for wastewater treatment. *Int. J. Miner. Metall. Mater.* **2023**, *30*, 177−191.

(35) Zhang, Y.; Zhang, H. B.; Wu, X. Y.; Deng, Z. M.; Zhou, E. G.; Yu, Z. Z. Nanolayered cobalt@carbon hybrids derived from metal-organic frameworks for microwave absorption. *ACS Appl. Nano Mater.* **2019**, *2*, 2325−2335.

(36) Cheng, Y.; Zhao, Y.; Zhao, H. Q.; Lv, H. L.; Qi, X. D.; Cao, J. M.; Ji, G. B.; Du, Y. W. Engineering morphology configurations of hierarchical flower-like MoSe$_2$ spheres enable excellent low-frequency and selective microwave response properties. *Chem. Eng. J.* **2019**, *372*, 390−398.

(37) Wei, S.; Shi, Z. C.; Li, X. S.; Chen, T.; Gao, H.; Chen, S. G. Bimetallic MOF-derived CoFe@nitrogen-doped carbon composites for wide bandwidth and excellent microwave absorption. *J. Alloys Compd.* **2022**, *910*, No. 164861.

(38) Pan, F.; Liu, Z. C.; Deng, B. W.; Dong, Y. Y.; Zhu, X. J.; Lu, W. Lotus leaf-derived gradient hierarchical porous C/MoS$_2$ morphology genetic composites with wideband and tunable electromagnetic absorption performance. *Nano-Micro Lett.* **2021**, *13*, 43.

(39) Wang, J. L.; Zhou, M.; Xie, Z. C.; Hao, X. Y.; Tang, S. L.; Wang, J. W.; Zou, Z. Q.; Ji, G. B. Enhanced interfacial polarization of biomass-derived porous carbon with a low radar cross-section. *J. Colloid Interface Sci.* **2022**, *612*, 146−155.

(40) Zhu, J.; Lan, D.; Liu, X.; Zhang, S.; Jia, Z.; Wu, G. Porous structure fibers based on multi-element heterogeneous components for optimized electromagnetic wave absorption and self-anticorrosion performance. *Small* **2024**, No. 2403689.

(41) Xie, Y. X.; Guo, Y. Y.; Cheng, T. T.; Zhao, L. B.; Wang, T.; Meng, A. L.; Zhang, M.; Li, Z. J. Efficient electromagnetic wave absorption performances dominated by exchanged resonance of lightweight PC/Fe$_3$O$_4$@PDA hybrid nanocomposite. *Chem. Eng. J.* **2023**, *457*, No. 141205.

(42) Xu, X. Q.; Ran, F. T.; Fan, Z. M.; Cheng, Z. J.; Lv, T.; Shao, L.; Xie, Z. M.; Liu, Y. Y. Acidified bimetallic MOFs constructed Co/N Co-doped low dimensional hybrid carbon networks for high-efficiency microwave absorption. *Carbon* **2021**, *171*, 211−220.

(43) Li, X.; Yin, X.; Song, C.; Han, M.; Xu, H.; Duan, W.; Cheng, L.; Zhang, L. Self-assembly core-shell graphene-bridged hollow MXenes spheres 3D foam with ultrahigh specific EM absorption performance. *Adv. Funct. Mater.* **2018**, *28*, No. 1803938.

(44) Cheng, J.; Zhang, H.; Ning, M.; Raza, H.; Zhang, D.; Zheng, G.; Zheng, Q.; Che, R. Emerging materials and designs for low- and multi-band electromagnetic wave absorbers: The search for dielectric and magnetic synergy. *Adv. Funct. Mater.* **2022**, *32*, No. 2200123.

(45) Zhang, K.; Liu, Y.; Liu, Y.; Yan, Y.; Ma, G.; Zhong, B.; Che, R.; Huang, X. Tracking regulatory mechanism of trace Fe on graphene electromagnetic wave absorption. *Nano-Micro Lett.* **2024**, *16*, 66.

(46) Wang, H. G.; Meng, F. B.; Li, J. Y.; Li, T.; Chen, Z. J.; Luo, H. B.; Zhou, Z. W. Carbonized design of hierarchical porous carbon/Fe$_3$O$_4$@Fe derived from loofah sponge to achieve tunable high-performance microwave absorption. *ACS Sustain. Chem. Eng.* **2018**, *6*, 11801−11810.

(47) Xu, C. C.; Ma, L.; Li, H. J.; Zhang, P.; Li, A. B.; Tan, W. J.; Zhang, Y. H.; Gong, C. H. Biomass derived PANI/BPC composite with enhanced polarization loss for efficient electromagnetic wave absorption. *Mater. Res. Bull.* **2024**, *176*, No. 112805.

(48) Pang, X. N.; Ye, L. D.; Li, X. J.; Yan, B. H.; Zhang, J. L.; Yang, X. Magnetic core-shell structure in-situ encapsulated in bamboo-derived carbon skeleton for efficient microwave absorption. *J. Alloys Compd.* **2021**, *888*, No. 161510.

(49) Li, X.; Cui, E. B.; Xiang, Z.; Yu, L. Z.; Xiong, J.; Pan, F.; Lu, W. Fe@NPC@CF nanocomposites derived from Fe-MOFs/biomass cotton for lightweight and high-performance electromagnetic wave absorption applications. *J. Alloys Compd.* **2020**, *819*, No. 152952.

(50) Zhang, Y. H.; Li, Y.; Liu, H. J.; Zhang, L.; Zhang, Y.; Xu, C. C.; Gong, C. H. Biomass-derived heterogeneous RGO/Ni/C composite with hollow structure for high-efficiency electromagnetic wave absorption. *Mater. Today Phys.* **2023**, *31*, No. 100966.

(51) Wang, L. X.; Guan, Y. K.; Qiu, X.; Zhu, H. L.; Pan, S. B.; Yu, M. X.; Zhang, Q. T. Efficient ferrite/Co/porous carbon microwave absorbing material based on ferrite@metal−organic framework. *Chem. Eng. J.* **2017**, *326*, 945−955.

(52) Shen, Z. J.; Yang, H. L.; Xiong, Z. Q.; Xie, Y.; Liu, C. B. Hollow core-shell CoNi@C and CoNi@NC composites as high-performance microwave absorbers. *J. Alloys Compd.* **2021**, *871*, No. 159574.

(53) Liu, Y.; Chen, Z.; Xie, W. H.; Song, S. K.; Zhang, Y.; Dong, L. J. In-situ growth and graphitization synthesis of porous $Fe_3O_4$/carbon fiber composites derived from biomass as lightweight microwave absorber. *ACS Sustainable Chem. Eng.* **2019**, *7*, 5318−5328.

(54) Cui, Y. H.; Yang, K.; Lyu, Y. T.; Liu, P. I.; Zhang, Q. Y.; Zhang, B. L. Hollow nitrogen-doped carbon nanofibers filled with $MnO_2$ nanoparticles/nanosheets as high-performance microwave absorbing materials. *Carbon* **2022**, *196*, 49−58.

(55) Wang, P.; Li, Z. C.; Cheng, L. F.; Ye, F.; Zhang, L. T. SiC/rGO core-shell nanowire as lightweight, highly efficient gigahertz electromagnetic wave absorber. *ACS Appl. Electron. Mater.* **2020**, *2*, 473−482.

(56) Xiong, X. H.; Zhang, H. B.; Lv, H. L.; Yang, L. T.; Liang, G. S.; Zhang, J. C.; Lai, Y. X.; Cheng, H. W.; Che, R. C. Recent progress in carbon-based materials and loss mechanisms for electromagnetic wave absorption. *Carbon* **2024**, *219*, No. 118834.

(57) Yan, H.; Lou, Z. C.; Xu, L.; Lv, H. L. Pore-regulation in 2D biochar-based flakes towards wideband microwave absorption. *Chem. Eng. J.* **2023**, *464*, No. 142568.

(58) Lv, H. L.; Ji, G. B.; Liu, W.; Zhang, H. Q.; Du, Y. W. Achieving hierarchical hollow carbon@Fe@$Fe_3O_4$ nanospheres with superior microwave absorption properties and lightweight features. *J. Mater. Chem. C* **2015**, *3*, 10232−10241.

(59) Cui, C.; Geng, L.; Jiang, S.; Bai, W. H.; Dai, L. L.; Ren, E. H.; Liu, L.; Guo, R. H. Architecture design of a bamboo cellulose/ $Nb_2CT_x$ MXene/ZIF-67-derived lightweight Co/$Nb_2CT_x$/carbon aerogel for highly efficient electromagnetic wave absorption, thermal insulation, and flame retardant. *Ind. Eng. Chem. Res.* **2023**, *62*, 8297−8311.

(60) Guo, L.; An, Q. D.; Xiao, Z. Y.; Zhai, S. R.; Cui, L.; Li, Z. C. Performance enhanced electromagnetic wave absorber from controllable modification of natural plant fiber. *RSC Adv.* **2019**, *9*, 16690−16700.

(61) Jia, Z.; Liu, J.; Gao, Z.; Zhang, C.; Wu, G. Molecular intercalation-induced two-phase evolution engineering of 1T and 2H-$MS_2$ (M = Mo, V, W) for interface-polarization-enhanced electromagnetic absorbers. *Adv. Funct. Mater.* **2024**, No. 2405523.

(62) Wen, J. H.; Lan, D.; Wang, Y. Q.; Ren, L. G.; Feng, A. L.; Jia, Z. R.; Wu, G. L. Absorption properties and mechanism of lightweight and broadband electromagnetic wave-absorbing porous carbon by the swelling treatment. *Int. J. Miner. Metall. Mater.* **2024**, *31*, 1701−1712.

(63) Chen, X.; Wang, Z.; Zhou, M.; Zhao, Y.; Tang, S.; Ji, G. Multilevel structure carbon aerogels with 99.999% electromagnetic wave absorptivity at 1.8 mm and efficient thermal stealth. *Chem. Eng. J.* **2023**, *452*, No. 139110.

(64) Xu, B. K.; He, Q. C.; Wang, Y. Q.; Yin, X. M. Hollow porous Ni@SiC nanospheres for enhancing electromagnetic wave absorption. *Ceram. Int.* **2023**, *49*, 21335−21345.

(65) Gu, W.; Sheng, J.; Huang, Q.; Wang, G.; Chen, J.; Ji, G. Environmentally friendly and multifunctional shaddock peel-based carbon aerogel for thermal-insulation and microwave absorption. *Nano-Micro Lett.* **2021**, *13*, 102.

(66) Chen, X. T.; Zhou, M.; Zhao, Y.; Gu, W. H.; Wu, Y.; Tang, S. L.; Ji, G. B. Morphology control of eco-friendly chitosan-derived carbon aerogels for efficient microwave absorption at thin thickness and thermal stealth. *Green Chem.* **2022**, *24*, 5280−5290.